

---



# 2-D Numerical Simulation of Differential Viscoelastic Fluids in a Single-Screw Continuous Mixer: Application of Viscoelastic Finite Element Methods

---

**ROBIN K. CONNELLY, JOZEF L. KOKINI**

*Department of Food Science, Center for Advanced Food Technology, Cook College, Rutgers University, New Brunswick, New Jersey 08901-8520*

Received: July 11, 2001

Accepted: October 8, 2002

**ABSTRACT:** Viscoelastic effects on mixing flows obtained with kneading paddles in a single-screw, continuous mixer were explored using 2-D finite element method numerical simulations. The single-mode Phan–Thien Tanner nonlinear, viscoelastic fluid model was used with parameters for a dough-like material. The viscoelastic limits of the simulations were found using elastic viscous stress splitting,  $4 \times 4$  sub-elements for stress, streamline upwind, and streamline upwind Petrov–Galerkin (SUPG). Mesh refinement and comparison between methods was also done. The single-screw mixer was modeled by taking the kneading paddle as the point of reference, fixing the mesh in time. Rigid

*Correspondence to:* Jozef L. Kokini; e-mail: kokini@aesop.rutgers.edu.

Contract grant sponsor: USDA National Research Initiative Competitive Grants Program.

Contract grant number: 2000-1768.

rotation and no slip boundary conditions at the walls were used with inertia taken into account. Results include velocity, pressure, and stress profiles. The addition of viscoelasticity caused the shear and normal stresses to vary greatly from the viscous results, with a resulting loss of symmetry in the velocity and pressure profiles in the flow region. © 2003 Wiley Periodicals, Inc. *Adv Polym Techn* 22: 22–41, 2003; Published online in Wiley InterScience (www.interscience.wiley.com). DOI 10.1002/adv.10038

**KEY WORDS:** FEM, Mixing, Modeling, Simulation, Viscoelastic properties

## Introduction

Use of high shear, single or twin blade, batch or continuous mixers for the processing of highly viscous materials is an important unit operation in the production of a wide variety of products, including adhesives, doughs, paints and coatings, candy, resins and rubbers, pet foods, pharmaceutical products, soaps, etc. Successful mathematical modeling and computer simulation of the flow and mixing in a mixing operation would be a cost effective way to obtain quantitative mixing parameters. It is far less expensive than machining and building mixer geometries and testing them for mixing ability. It is also one of the most effective ways to gain insights about the operation of a system where adequate physical measurements to characterize the system are not readily possible, such as in an opaque dough, paint, gum, resin, or rubber. One can perceive mathematical simulation as an effective way to nonintrusively probe a process and learn about what goes on inside the material being mixed. However, modeling of mixing flows in realistic mixers, especially with viscoelastic materials, such as dough or synthetic polymers, is challenging due to the complex geometry and rheology. These geometries may also lead to many singularities that cause the modeling methods to break down with viscoelastic fluid models. In fact, use of viscoelastic fluid models in mixing simulations is rare. Finite element method (FEM) modeling of a simple paddle impeller in a cylindrical vessel for an Oldroyd-B fluid was done by Ann-Archard and Boisson<sup>1</sup> using the Galerkin method and  $4 \times 4$  Streamline upwind (SU) and compared to similar experimental velocity data.<sup>2,3</sup> The 2-D assumption in this case was found to give simulation results that agreed well with the experimental results. Petera and Nassehi<sup>4</sup> used the Maxwell and the Phan–Thien Tanner (PTT) models in a simulation of a free surface viscoelastic flow for rubber in

an internal mixer. The modeling was done using Galerkin FEM with SU Petrov–Galerkin (SUPG). The free surface was handled by a modified pseudodensity method that eliminated the convection terms in the free surface model equations and thus the need for artificial physical parameters. The results were validated with a novel experimental rig.<sup>5</sup> Boundary element analysis of a simple mixer with a Maxwell linear viscoelastic fluid model found the viscoelasticity to only influence the evolution of stress at the rotor and walls, but not the velocity profile.<sup>6</sup> Dhanasekharan and Kokini<sup>7</sup> modeled the 3-D flow of a single mode PTT fluid in the metering zone of a completely filled single-screw extruder. It was modeled by means of a stationary screw and rotating barrel. The leakage flow between the screw and barrel was neglected, leading to minimal effects due to viscoelasticity being observed.

There are many computational fluid dynamics (CFD) approaches to discretizing the equations of conservation of momentum, mass, and energy together with the constitutive equation that defines the rheology of the fluid being modeled and the boundary and initial conditions that govern the flow behavior in a particular mixer. The most important of these are finite difference (FDM), finite volume (FVM), and finite element (FEM). Others such as spectral schemes, boundary element methods, and cellular automata are used in CFD but their use is limited to special classes of problems.<sup>8</sup> The modeling of viscoelastic fluid flows has been most successful with FEM. During early attempts at modeling viscoelastic fluid flow with FEM, the solutions invariably became unstable at unrealistically low values of the Weissenberg number ( $Wi$ ) or the related Deborah number ( $De$ ).<sup>9</sup> This problem, called the “high Weissenberg number problem,” is for the most part due to the hyperbolic character of the advective term in the viscoelastic constitutive equations, which increases in importance with increasing  $De$ .<sup>10</sup> This is especially apparent at geometrical singularities such as

sudden contractions, sudden changes in boundary conditions as represented by the stick-slip problem, and flow around a sphere or cylinder, all of which are considered benchmark problems in viscoelastic flow simulation.<sup>11</sup> At singularities, which are found in most practical problems including the flow in mixers, there are stress concentrations that increase to infinity as the mesh is refined. In addition, the presence of normal stresses gives rise to very thin boundary layers in complex flows. The high stress gradients in these layers are believed to be the cause of problems for most numerical methods.<sup>10</sup>

In order to ease the problems caused by the high stress gradients, Marchal and Crochet<sup>12</sup> introduced the use of  $4 \times 4$  subelements for the stresses, which was later proven to be optimal.<sup>13</sup> These bilinear subelements smoothed the mixed method solution of the Newtonian stick-slip problem, as well as aided in the convergence of the viscoelastic problem. In order to deal with the hyperbolic nature of the advective term of the constitutive equation, Marchal and Crochet<sup>12</sup> implemented two different modifications to the standard mixed Galerkin method: the consistent SUPG formulation<sup>14</sup> and the nonconsistent SU method. The basic idea of SU is to add artificial diffusivity (or viscosity) that acts only in the flow direction. Extended to a Petrov–Galerkin formulation, the standard Galerkin weighting functions are modified to weigh the element upwind of the node more heavily than the downwind element. Because the artificial diffusivity is applied only in the flow direction, crosswind distortions are eliminated. When the weighting is consistent across all terms, there is no overall artificial diffusivity effect.

However, when originally applied to the stick-slip problem by Marchal and Crochet,<sup>12</sup> SUPG still failed when the constitutive equations were coupled with the equations of motion and the incompressibility constraint. Therefore, they applied the artificial diffusivity only to the advective term of the constitutive equation. This nonconsistent application of the SU method, when combined with the use of  $4 \times 4$  subelements for stress, had great success, reaching  $De$  numbers as high as 64 for a circular contraction. Unfortunately, the nonconsistent SU does give rise to artificial stress diffusion along the streamlines. There has been some question of the importance of the artificial stress diffusion along the streamlines, with Luo and Tanner<sup>15</sup> claiming it actually changed the nature of the constitutive equation and affected the results at any level of mesh refinement. However, while the error of the stress term is of  $O(h)$  or worse<sup>16,17</sup> where  $h$  is on the order of the mesh size, advection dominates

diffusion as the mesh size decreases so that the artificial diffusivity term becomes negligible.<sup>18</sup> Therefore, the accuracy of problems solved using the SU  $4 \times 4$  method must be verified on at least two, preferably three, finite element meshes of decreasing element size.<sup>17,19</sup> Further work with SUPG showed that while it is not as robust where there are stress singularities, it is more accurate (to  $O(h^3)$ ), especially for unequal element sizes, and converges faster than SU.<sup>16,17</sup>

The success of the artificial diffusivity concept to deal with the “high Weissenberg problem” led to other methods as well. One of the most successful methods is known as elastic viscous stress splitting (EVSS). This is done by splitting the stress tensor into the sum of the viscoelastic and Newtonian contributions, which regularizes the behavior of the constitutive equations. The Newtonian contribution is given by  $2\eta D$ , where  $D$  is the strain rate tensor and  $\eta$  is the Newtonian (or solvent) viscosity.  $D$  is considered as an additional unknown that is approximated with a least square method.<sup>20–22</sup>

In light of these advances in using differential viscoelastic models in FEM simulations and the lack of published examples using this technology with highly viscous, viscoelastic materials in mixers, the application of these techniques to the development of flow profiles for a dough-like material in a 2-D simplified mixer that can be used to mix dough is explored.

---

## Materials and Methods

### PROBLEM DESCRIPTION AND MESH DEVELOPMENT

The 2-D geometry for a single-kneading paddle in a 2" circular barrel with complete fill is shown in Fig. 1. Flow occurs in the shaded area between the barrel and the paddle. The paddle shape was calculated using the equations of Booy<sup>23</sup> for a 2", dual lobed, self-wiping, twin-screw mixer, with  $\alpha$  and  $\beta$  as shown in Fig. 1. The paddles used were actually of the 2" Continuous Processor of Readco Manufacturing (York, PA), which is a low pressure, corotating, twin-screw mixer used in such diverse applications as dough mixing, polymeric condensation and other chemical reactions involving polymers, incorporation of light weight powders into highly viscous materials such as bulk molding compounds and rubbers, chocolate conching, production of pharmaceutical pastes for pill formulation, etc. The

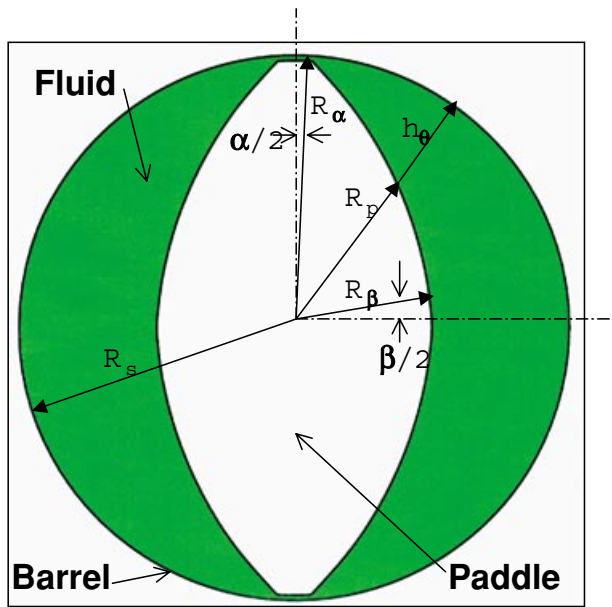


**FIGURE 1.** Geometry used in the simulations<sup>23</sup> where  $\alpha = 4.7^\circ$  (0.082 rad.),  $\beta = 9.6^\circ$  (0.167 rad.),  $R_s = 2.54$  cm (barrel radius),  $R_\beta = 1.269$  cm,  $R_\alpha = 2.4895$  cm, and  $C_L = 3.809$  cm (twin shaft clearance). For  $(\beta/2) \leq \theta \leq (90 - \alpha/2)$ ,  $R_p = R_s - h_\theta$  (paddle radius) and  $h_\theta = R_s(1 + \cos(\theta - \beta/2)) - (C_L^2 - R_s^2 \sin^2(\theta - \beta/2))^{0.5}$ .

geometry seen here is similar to that seen in the kneading zone of a single-screw extruder. However, since the velocity in the  $z$  direction is not taken into account and the pressure is low, this simulation more realistically models a batch mixer consisting of a paddle in a cylindrical tank.<sup>3</sup> To fix the mesh in time, the paddle is taken as the frame of reference with the barrel rotating in a counterclockwise direction. For a cylindrical system, Rauwendaal et al.<sup>24</sup> found the pressure and velocity gradients to be the same for either the barrel rotating or the paddle rotating, except for the effect of centrifugal and Coriolis forces on the boundary conditions. In order to take into account centrifugal and Coriolis forces, rigid rotation of the entire system is assumed at a speed of  $-\Omega$ , which is in a clockwise direction. The Coriolis force, which is a deflecting force due to flows in both the radial and angular directions, and the centrifugal force, which is in the radial direction resulting from the angular velocity, are pseudoforces due to being in a noninertial reference frame. A measure of the importance of the Coriolis forces is the Rossby number, which is of the order of the ratio of the blade radius to the channel height in an extruder. If the Rossby number  $\gg 1$ , Coriolis forces

are of negligible effect, while at around unity they are of mixed effect, and are dominate at  $\ll 1$ .<sup>25</sup> Using a generalized Newtonian fluid in a single-screw extruder Spalding et al.<sup>26</sup> found centrifugal and Coriolis forces with a Rossby number of  $\sim 10$  to be negligible. In our case it varies from a minimum of 1 in the middle of the channel to a value of 100 in the gap, and therefore the Coriolis force may have some non-negligible effects. Simulations at 1 and 100 rpm without rigid rotation were done in order to explore the importance of these pseudoforces in this geometry. Inertia was taken into account with density set at  $1.204 \text{ gm/cm}^3$ , which is the density of 43.2% moisture flour-water dough. The tangential velocity of the barrel was set to  $\Omega R_s$ . No slip conditions were used at the barrel and paddle walls.

The meshes used in this work were created using Gambit (Fluent). The 1480 element mesh pictured in Fig. 2 is representative of the meshes. The 360 element mesh was designed to be coarse with increased

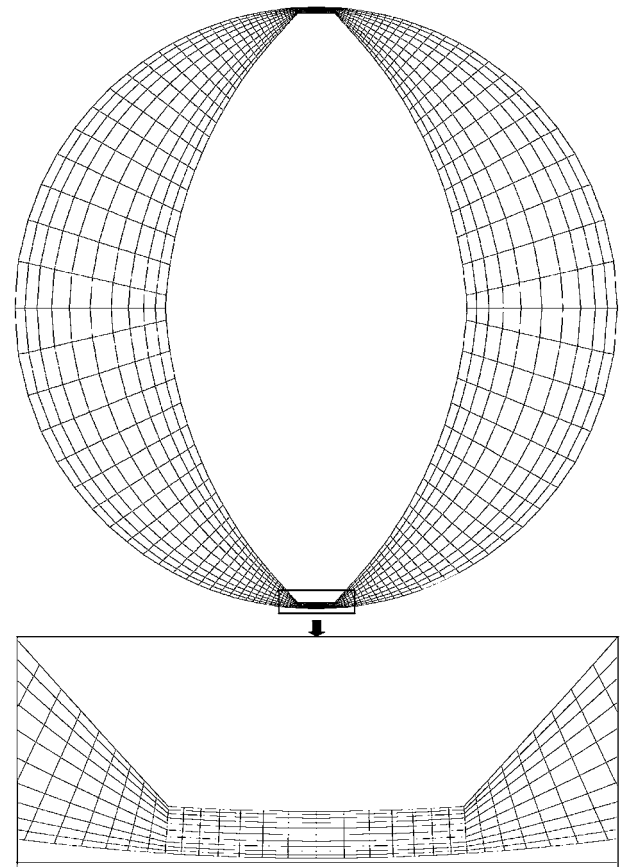


**FIGURE 2.** An example of the meshes used in the simulations. It is the 1480 element mesh.

refinement in areas of high gradients as indicated by experience. In this case it is at the wall, in the gap, and near the entrance to the gap at the blade tip. The ratios used in the mesh spacing were chosen to meet this goal while at the same time creating quadrilateral elements as near to square as possible as indicated by the mesh tests described later. Ideally, refinement is done by dividing elements, but keeping the original nodes in the same place. The jump from 360 to 600 doubled the elements on the sides of the paddles. After that the meshes were refined by adding elements as well as by setting the spacing ratios such that the element shape is optimized according to the mesh tests. Direct doubling quickly makes the number of elements enormous and the element shape deteriorates.

The 360 and 600 element meshes have 5 elements across the channel, including across the gap, while the 1480 and 2080 have 10. The 3360 element mesh has 12. A ratio in spacing between nodes of 1.2 (360 and 600) or 1.1 (rest) from walls to the center of channel was used (e.g., if the spacing between the wall node and the 2nd node is 1, then the spacing between the 2nd node and the 3rd node will be 1.1, between 3rd and 4th 1.21, etc.) The 360 and 600 element meshes have 26 and 50 elements across the paddle sides and 10 across the paddle tip with a 1.2 ratio from the paddle tip. The paddle sides for the 1480 element mesh has 60 elements (1.1 ratio from tip) while the 2080 element mesh has 90, and the 3360 element mesh has 120 with a ratio from the paddle tip of 1.05 on the wall and 1.1 on the paddle. The paddle tips contain 14 elements (1480 and 2080) or 20 (3360) with ratio of 1.1 from the edge to the center of the tip.

Gambit offers a variety of mesh tests to evaluate the quality of meshes for use in FEM. Ideally,

perfectly square (or perfectly triangular) 2-D elements are needed for the most effective use of FEM. However, realistic geometries do not lend themselves to the use of only perfect elements. One of the goals in mesh creation is to keep the shape of the elements as close to ideal as possible, while still accurately representing the real geometry. These quality tests are measures of how well a given mesh has succeeded in meeting this goal. Equiangle skew, which looks at how close the angles of each mesh quadrilateral are to 90°, is defined as

$$Q_{EAS} = \max \left\{ \frac{\theta_{\max} - 90}{90}, \frac{90 - \theta_{\min}}{90} \right\}$$

where  $\theta_{\max}$  and  $\theta_{\min}$  are the largest and smallest angle respectively in degrees. Stretch ratio, which looks at how close each mesh quadrilateral is to an equilateral element, is defined as

$$Q_s = 1 - \sqrt{\frac{2[\min(s_1, s_2, s_3, s_4)]^2}{\max[d_1, d_2]^2}}$$

where  $s_i$  indicates side and  $d_i$  indicates diagonal. For both of these tests, a value of 0 indicates a perfect element while a value of 1 indicates a degenerate element. They combine to give a good overall picture of the quality of the meshes in this work.<sup>27</sup>

As shown in Table I, all mesh quadrilaterals fall into the excellent (<0.25) or good (<0.5) range for equiangle skew, although only the 2080 element mesh is considered a high quality mesh with an average value <0.1. The 360 element and 1480 element meshes score only fair for stretch ratio, while the 2080 element mesh again scores the best. Unfortunately, the elements that scored only good according to the

**TABLE I**  
**Results of Mesh Tests**

Test	Elements in the Mesh				
	360	600	1480	2080	3360
Equiangle skew					
<0.1	35.6%	32.7%	46.2%	56.1%	54.9%
<0.25	91.1%	87.3%	94.0%	88.2%	86.6%
<0.5	100%	100%	100%	100%	100%
Stretch					
<0.25	1.1%	40.7%	14.9%	49.8%	43.6%
>0.5	51.1%	12.0%	50.3%	22.1%	16.4%

mesh tests occur near the blade tips, where instability will occur due to the high gradients at the wall and the blade surface, as well as the stress concentration at the corner. The 2080 element mesh had the best-shaped elements in these regions, and the result is a more stable solution.

**FLUID MODEL AND FLOW PARAMETERS**

A typical application of this type of mixer is the processing of dough. Therefore, the PTT nonlinear viscoelastic model<sup>28</sup> was chosen for its ability to model the behavior of a model flour–water dough as well as its relatively good behavior in FEM simulation. The PTT constitutive model takes the following form

$$\exp\left[\varepsilon \frac{\lambda}{\eta_1} \text{tr}(\mathbf{T}_1)\right] \mathbf{T}_1 + \lambda \left[ \left(1 - \frac{\xi}{2}\right) \overset{\nabla}{\mathbf{T}}_1 + \frac{\xi}{2} \overset{\Delta}{\mathbf{T}}_1 \right] = 2\eta_1 \mathbf{D}$$

The parameters are based on those of Dhanasakaran et al.<sup>29</sup> as follows: the partial viscosity  $\eta_1 = 88888.9$ , poise  $\varepsilon = 0.08$ , and  $\xi = 0.01$ . The relaxation time  $\lambda$  is evolved from a value of zero (the Newtonian case) to the point where the simulation diverges and will

no longer give a solution. The stress was considered to be divided with a purely viscous component  $\mathbf{T}_2 = 2\eta_2 \mathbf{D}$ , such that the total stress  $\mathbf{T} = \mathbf{T}_1 + \mathbf{T}_2$  with  $\mathbf{D}$  being the rate of deformation. The resulting viscosity ratio was set to  $\eta_1/(\eta_1 + \eta_2) = 1/9$ . The steady shear profiles for several of the values of the relaxation time used in this work are shown in Fig. 3. The shear thinning behavior of these models is exhibited only in a very limited range of shear rates that range from around 2–200  $\text{s}^{-1}$  for  $\lambda = 0.5$  s to about 0.001–0.1  $\text{s}^{-1}$  for  $\lambda = 1000$  s. We shall see later that the shear rate range observed in the mixer at 1 rpm was from around 0.1 to 30  $\text{s}^{-1}$ , which is in the shear thinning range of most of the models considered. Figure 3 also shows that the 4 mode dough model of Dhanasekaran et al.<sup>29</sup> is very similar in viscosity to the single mode PTT models used in this work in the shear rate range of interest, especially at the lower relaxation times.

Typically in a mixer, the Deborah Number, which is defined as the ratio of the characteristic material time to the characteristic process time, is taken to be  $De = \lambda\Omega$  and is the definition we use here.<sup>30</sup> The Weissenburg number, which is defined as the ratio of the elastic force to the viscous force, is described

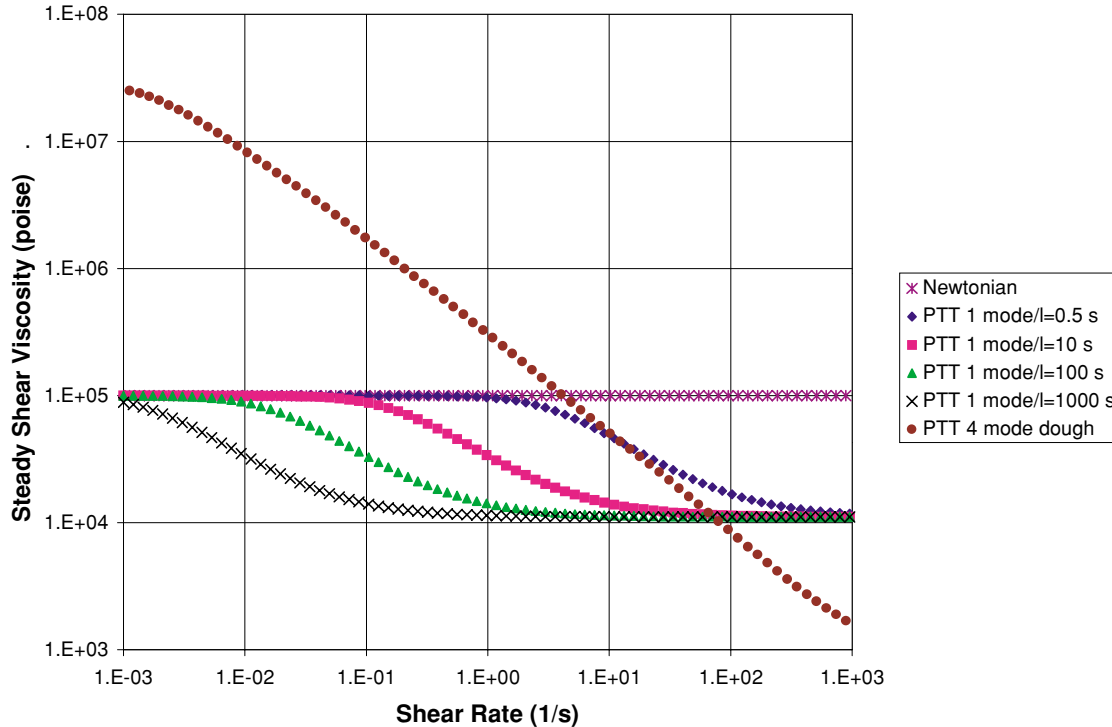


**FIGURE 3.** Steady shear profiles for single mode PTT models used in the 2-D simulations with the four mode PTT dough model of Dhanasekharan et al.<sup>29</sup> as a reference.

as  $Wi = (\Psi_1/\eta)\Omega$ , where  $\Psi_1$  is the primary normal stress coefficient and  $\eta$  is the viscosity.<sup>30</sup> The primary normal stress coefficient is defined as

$$\Psi_1 \equiv \frac{-(\tau_{11} - \tau_{22})}{\dot{\gamma}^2} = \frac{N_1}{\dot{\gamma}^2}$$

under steady simple shear flow conditions. It is related empirically to the shear rate ( $\dot{\gamma}$ ) by the expression<sup>30</sup>  $\Psi_1 = m'|\dot{\gamma}|^{n'-2}$ . In the case of the PTT model,  $\eta$  and  $\Psi_1$  are shear rate dependant, so  $Wi$  does not have a global meaning but only a local. The primary normal stress coefficient ( $\Psi_1$ ) for the PTT model in viscometric flow<sup>28</sup> is given by

$$\Psi_1 = 2 \frac{\eta_1 \lambda}{1 + \xi(2 - \xi)\lambda^2 \dot{\gamma}^2}$$

The viscometric flow relations will be used as estimates of the actual values during mixing and simulation.

## SIMULATION METHODOLOGY

For flow problems of viscoelastic fluids of the differential type, Polyflow first develops a mixed Galerkin formulation of the governing equations. For this steady-state, 2-D isothermal flow where the domain  $\chi$  is the space between the paddle and the barrel, the viscoelastic extra-stress, velocity, and pressure are approximated respectively by means of the finite expansions:

$$\mathbf{T}_1^a = \sum_{i=1}^{N_T} T_1^i \phi_i \quad \mathbf{v}^a = \sum_{j=1}^{N_v} v^j \psi_j \quad p^a = \sum_{k=1}^{N_p} p^k \pi_k$$

where  $\phi_i$ ,  $\psi_j$ , and  $\pi_k$  represent given finite element basis functions, while  $T_1^i$ ,  $v^j$ , and  $p^k$ -are unknown nodal values. Substituting the approximation into the isothermal governing equations, using the mixed Galerkin method, the following set of equations is obtained:

$$\int_{\chi} \phi_i \left[ \exp \left[ \varepsilon \frac{\lambda}{\eta_1} \text{tr}(\mathbf{T}_1) \right] \mathbf{T}_1^a + \lambda \frac{\delta \mathbf{T}_1^a}{\delta t} - 2\eta_1 \mathbf{D}^a \right] d\chi = 0$$

(constitutive equation)

$$\int_{\chi} \left\{ \psi_j \rho \left[ \frac{d\mathbf{v}^a}{dt} - \mathbf{f} \right] + \nabla \psi_j^T \cdot [-p^a \mathbf{I} + 2\eta_2 \mathbf{D}^a + \mathbf{T}_1^a] \right\} d\chi$$

$$= \int_{\partial\chi} \psi_j \boldsymbol{\sigma} \cdot \mathbf{n} ds \quad (\text{conservation of momentum})$$

$$\int_{\chi} \pi_k [\nabla \cdot \mathbf{v}^a] d\chi = 0 \quad (\text{conservation of mass})$$

where  $\frac{\delta \mathbf{T}_1^a}{\delta t} = \frac{\xi}{2} \overset{\nabla}{\mathbf{T}}_1 + (1 - \frac{\xi}{2}) \overset{\nabla}{\mathbf{T}}_1$  and  $\mathbf{f}$  contains the Coriolis and centrifugal terms. When  $\lambda$  vanishes, the constitutive equation reduces to the generalized Newtonian case.<sup>31</sup> Because of the hyperbolic nature of the  $\lambda \mathbf{v} \cdot \nabla \mathbf{T}_1$  term from the upper- and lower-convected derivatives of the extra-stress  $\overset{\nabla}{\mathbf{T}}_1$ , the accuracy and stability of the mixed Galerkin formulation deteriorates as the elasticity number increases in flows with boundary layers or singularities.<sup>10</sup> The numerical results can then be stabilized by the use of viscoelastic extra-stress interpolations such as SU or SUPG. The most robust technique, SU, is done by applying an artificial diffusivity  $\mathbf{K} = \bar{k} \frac{\mathbf{v} \mathbf{v}}{\mathbf{v} \cdot \mathbf{v}}$  to the hyperbolic term only in the stream-wise direction. The discrete constitutive equation then becomes:

$$\int_{\chi} \phi_i \left[ \mathbf{A}(\mathbf{T}_1^a, \lambda) \cdot \mathbf{T}_1^a + \lambda(\dot{\gamma}) \frac{\delta \mathbf{T}_1^a}{\delta t} - 2\eta_1 \mathbf{D}^a \right] d\chi$$

$$+ \int_{\chi} \frac{\lambda \bar{k} \mathbf{v}^a}{\mathbf{v}^a \cdot \mathbf{v}^a} (\mathbf{v}^a \cdot \nabla \mathbf{T}_1^a) \cdot \nabla \phi_i d\chi = 0$$

where  $\bar{k}$  is a scalar on the order of the mesh size.<sup>12</sup> While this technique gives rise to artificial extra-stress diffusion along the streamlines, the importance of stress diffusivity decreases when the finite element mesh is refined.<sup>17</sup> Therefore, five meshes of decreasing size were used to verify the results. In contrast, SUPG applies  $\mathbf{K}$  to all the terms in the discrete constitutive equation, eliminating the artificial diffusion.<sup>14</sup>

The viscoelastic extra-stress field interpolation techniques used in this work are elastic-viscous stress splitting (EVSS) and  $4 \times 4$  bilinear subelements for the stress. In EVSS, the stress tensor is split into elastic and viscous components. When the  $\mathbf{T} = \mathbf{T}_1 + \mathbf{T}_2$  form of the stress tensor is used, the convected derivative of the rate of strain emerges, which requires a second-order derivative of the velocity field. To overcome this,  $\mathbf{D}$  is considered an unknown

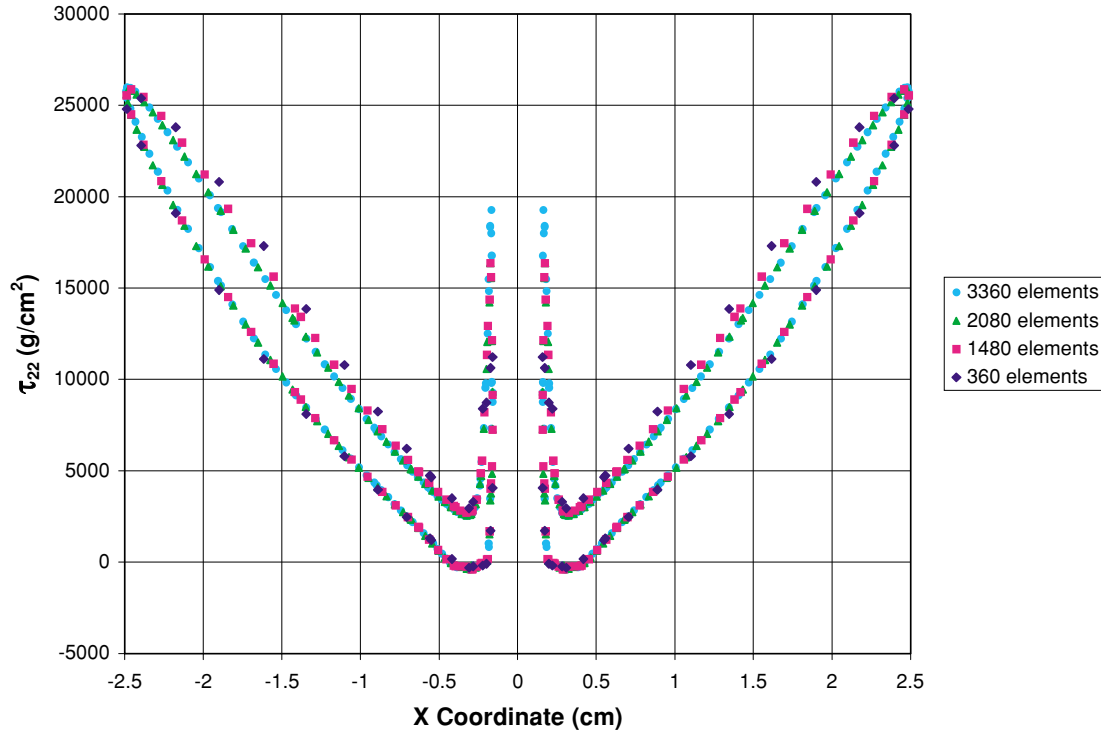


**FIGURE 4.** Normal stress  $\tau_{22}$  during mesh refinement for the PTT Model with  $\lambda = 100$  s on a circle of radius 2.489 cm.

and is obtained by a least squares approximation using the definition  $\mathbf{D} \equiv \frac{1}{2}[(\nabla \mathbf{v}) + (\nabla \mathbf{v})^T]$ .<sup>20,22</sup> The modified discrete constitutive equation and strain rate equation are as follows:

$$\int_{\chi} \phi_i \left[ \mathbf{A}(\mathbf{T}^a, \lambda) \cdot \mathbf{T}^a + \lambda(\dot{\gamma}) \left[ \frac{\delta \mathbf{T}^a}{\delta t} + 2\eta_1 \overset{\nabla}{\mathbf{D}}^a \right] \right] d\chi = 0$$

$$\text{and } \int_{\chi} \xi_i \left[ \mathbf{D}^a - (\nabla \mathbf{v}^a + \nabla^T \mathbf{v}^a)/2 \right] d\chi = 0$$

Alternatively, the solution can be stabilized by dividing each quadrilateral in the mesh into 16 bilinear subelements for calculating the stress.<sup>12</sup>

An iterative technique called evolution was used to gradually introduce the source of the instability into the solution. For differential, viscoelastic problems, evolution is usually done on either the relaxation time ( $\lambda$ ) or the mixing speed ( $\Omega$ ). This gives gradually increasing values of  $De$ . In this case it has been chosen to evolve  $\lambda$  at a range of fixed mixing speeds that go from a very low value of 1 rpm, which is in effect creeping flow, to a more typical speed for the mixer on which this simulation is based of 100 rpm. Then it is possible to see what

level of  $\lambda$  can be achieved at each speed, using the above numerical techniques. Evolution is applied to the relaxation time such that  $\lambda_i = f(S_i) \times \lambda_{\max}$ , where  $f(S_i) = S_i = (S_{i-1} + \Delta S_i)$  where  $S_0 = 0$  and  $S_{\text{final}} = 1$  and  $\Delta S_0 = 0.0001$ . Then the solution is obtained using Newton's iterative scheme with the converged solution of the previous step used as the initial guess when available. If the solution converges  $\Delta S_i = \Delta S_{i-1} \times 1.5$ . If the solution diverges,  $\Delta S_i = \Delta S_i/2$  and the iteration is re-done until  $\Delta S_i$  is

**TABLE II** Analysis of Mesh Refinement Error of  $\tau_{22}$  at 1 rpm with  $\lambda = 100$  s

Test	Elements in the Mesh		
	360	1480	2080
Pearson correlation coefficient ( $R$ )	0.9735	0.9908	0.9953
Without tip elements	0.9950	0.9994	0.9997
$R^2$	0.9477	0.9817	0.9906

Data read at points located on a circle of 2.489 cm are compared with linear estimates of data from the 3360 mesh at the same points.

**TABLE III**  
Limits of  $De$  Reached by Several Methods Used in Viscoelastic Simulations During Mesh Refinement at 1 rpm

Mesh Size	EVSS SUPG		4 × 4 SUPG		EVSS SU		4 × 4 SU	
	$\lambda$ (1 rpm)	$De$						
360 elements	0.327	0.034	0.23	0.024	651.04	68.2	1000	104.7
600 elements	0.178	0.019	1.04	0.109	14.12	1.47	23.4	2.45
1480 elements	0.089	0.009	0.089	0.009	0.73	0.076	131.78	13.8
2080 elements	–	–	0.066	0.007	0.79	0.082	543.58	56.9
3360 elements	–	–	–	–	0.58	0.061	110.32	11.6

less than a minimum  $\Delta S_{\min} = 1 \times 10^{-5}$  and the simulation stops.<sup>31</sup>

## Results and Discussion

### VISCOELASTIC LIMITS AND ACCURACY OF SIMULATION RESULTS

The coarsest mesh of 360 elements is somewhat inaccurate, but by the time the mesh size reached 1480 elements, the discretization error is minimal. The main difference between meshes with the viscoelastic fluids is the magnitudes of the pressure, shear stress, and, in particular, normal stresses calculated at the corner singularity as shown in Fig. 4. The variation in the values of normal stress  $\tau_{22}$  with a relaxation time of 100 s at the blade surface is the worst case of the results read on a circle of radius 2.489 cm. (Note that the data on this and subsequent graphs is read where a circle of the given radius crosses a mesh element. The  $x$ -axis is the  $x$ -coordinate of the data points with the origin the barrel center. Most  $x$  values will generate two data points at the corresponding positive and negative  $y$  positions.) Statistical tests of the equality of linear estimates of 3360 element mesh values with the actual values from the 360, 1480, and 2080 element meshes are shown in Table II. The square of the Pearson correlation coefficient ( $R^2$ ) of all three meshes to the 3360 element mesh is adequate. If the elements within 0.04 cm of the tip are disregarded, the results are nearly exact for the 1480 and 2080 element mesh, indicating that artificial stress diffusion is negligible throughout most of the flow domain.

Coarser meshes allowed convergence at higher  $De$  since effect of the discontinuity is smoothed. This mesh refinement effect has been noted by other

authors.<sup>22</sup> The more accurate SUPG technique is not adequate for this geometry because of the corner singularity at the blade tip, as is demonstrated in Table III. The less computationally intensive EVSS technique is also not as effective as using 4 × 4 bilinear subelements for stress. Therefore, the 4 × 4 SU technique was determined to be the method necessary to solve this problem. Even this technique was unable to reach the desired relaxation time of 1000 s at low rpm values. The excellent quality of the 2080 element mesh is demonstrated by the high relaxation time it is able to achieve in relation to the other meshes before the solution diverges. Instabilities at the start of evolution with the higher speeds necessitated the use of different parameters for the evolution procedure. A  $\Delta S_{\min}$  of  $1 \times 10^{-5}$  used 1 and 10 rpm while a  $\Delta S_{\min}$  of  $1 \times 10^{-6}$  used 60 and 100 rpm.

At the high rpm values that are more representative of the actual conditions found in this type of mixer, the instabilities in the calculations and some of the effects of the viscoelasticity seem to disappear as seen in Table IV. At 1 and 10 rpm, the calculations are highly unstable and able to achieve a maximum  $De$  of only 13.5. However, at 60 rpm, while there is some instability in the calculations at the start of evolution, the desired maximum relaxation time of 1000 s

**TABLE IV**  
Limits of  $De$  Reached at Several Blade Speeds Using the 1480 Element Mesh and 4 × 4 SU

Blade Speed	$\lambda$	$De$
1 rpm	131.78	13.8
10 rpm	12.8	13.4
60 rpm	1000	6283
100 rpm	1000	10472

1000 was the highest  $\lambda$  attempted.

is achieved. The last evidence of instability in the 60 and 100 rpm simulations occurs at  $De \approx 13.5$ . This is at the same  $De$  at which the 1 rpm and 10 rpm simulations broke down with this mesh. One possible reason that the higher rpm simulations were able to go beyond  $De = 13.5$  is the high value of the shear rates throughout the flow at those velocities. The shear rate range seen at 100 rpm is on the order of 10–1000 1/s as shown in Fig. 12. From the steady shear profiles of the PTT constitutive models shown in Fig. 3, it becomes evident that the shear thinning region would be of consequence with only the very smallest values of the relaxation time, where in fact the simulation did show evidence of instability. For the higher values of the relaxation time, the behavior of the Newtonian component of the viscosity dominates the simulation, thus stabilizing the solution and allowing the high  $De$  values that were achieved. Another way to think about this is to note that when the  $De$  is very high, either the characteristic material time is long or the characteristic process time is short or both. In either case, the material will not have time to relax and will follow its unrelaxed behavior profile. In this case, that is the behavior of the Newtonian component.

Another possible explanation for the behavior of the simulation at 100 rpm is that at higher velocities, the inertial forces come to dominate the elastic forces generated in the flow. A measure of the importance of elastic effects on mixing flow is the elasticity number ( $El$ ) defined as  $El = Wi/Re = \Psi_1/(\rho D^2)$  where  $D$  is the blade diameter and  $\rho$  is the fluid density. When  $El > 0.25$ – $0.5$ , elastic forces have been found to dominate the inertial forces, causing complete flow reversal the secondary flow profile in some mixer geometries.<sup>30,32,34</sup> In our case, when  $\lambda = 100$  s the  $El \ll 0.25$  at 100 rpm in the high shear regions and  $El \gg 0.5$  at 1 rpm throughout most of the flow domain, indicating that elasticity dominates at the low speed and inertia is important in high shear regions near the blade tip at the high speed. The effect of the inertia dominating the flow in the gap region is to dampen the viscoelastic effects and therefore stabilize the solution.

The centrifugal and Coriolis forces, which were included through use of rigid rotation, were a factor at high values of the relaxation time. For the PTT model at 1 rpm and  $\lambda = 100$  s, they changed the stresses about 13%, the velocity magnitude by an average of 0.4%, and shear rate and pressure by

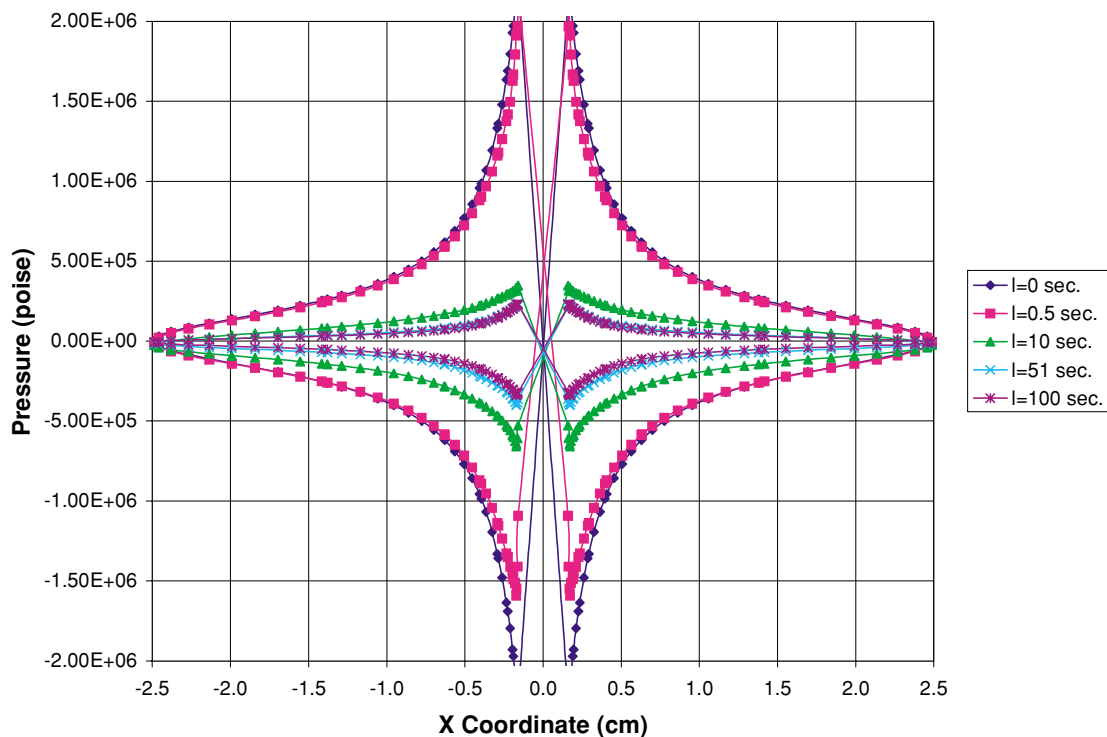


**FIGURE 5.** Pressure profiles at 1 rpm on the 2.489 cm radius circle with the 1480 element mesh for the PTT at several relaxation times.

an average of 2–3%. At an equivalent  $De$  with  $\lambda = 1$  s at 100 rpm they changed the solution only negligibly. No change in any variable was detected at 1 rpm in simulations using a Newtonian fluid or a shear thinning Bird–Carreau generalized Newtonian fluid. A side benefit of including the Coriolis and centrifugal forces with the PTT model fluid was that they had a stabilizing effect on the solution. Without rigid rotation, the maximum  $De$  achieved was only 13.4 at 100 rpm, while at 1 rpm it was only possible to reach that  $De$  level by using the more effective, but more computationally expensive 2080 element mesh.

**VISCOELASTIC EFFECTS**

The pressure variation profiles at 1 rpm for a series of relaxation times read on a circle of radius 2.489 cm are shown in Fig. 5, where the pressure value of zero is equivalent to ambient. These profiles are representative of the overall mapping of the pressure, since the pressure varies mainly with the angle from the center of rotation. It is interesting to

note that at a relaxation time of 0 s where the PTT model is equivalent to the Newtonian model, the pressure on the front and back of the blade is equal and opposite. However, as the relaxation time increases, two changes are observed: the magnitude of the pressure drops and there is a loss of symmetry in the profile. The change in magnitude was observed for purely shear thinning materials as shown in Fig. 6 for a series increasingly shear thinning Bird–Carreau viscous constitutive model fluids, but not the loss of symmetry between the front and back of the blades. Therefore, it appears that the loss of symmetry in the pressure differential between the front and back of the blades is a purely viscoelastic effect. Note also that at a relaxation time of 0.5 s, the asymmetry of the PTT fluid is of a different form from that seen at the higher relaxation times.

Related to effect on the pressure profiles, a loss of symmetry with increasing viscoelasticity is also evident in the velocity distributions. The velocity profile in the rotating reference frame is the secondary profile since the primary tangential components of the velocity were removed. It has been shown that

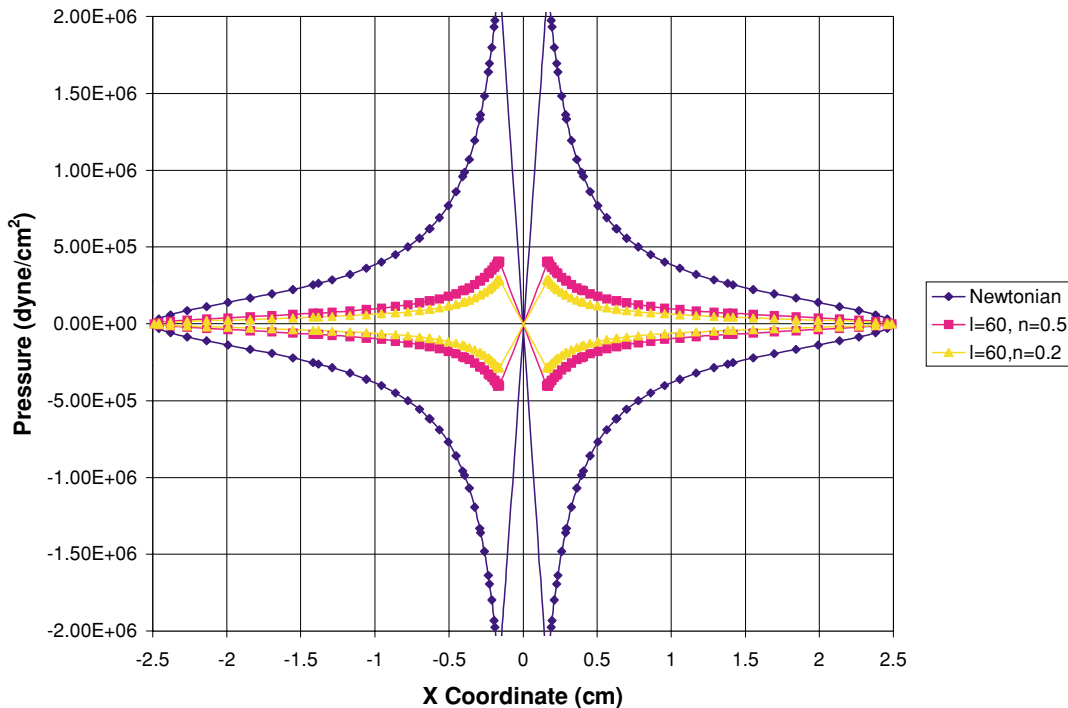


**FIGURE 6.** Pressure profiles at 1 rpm on the 2.489 cm radius circle for the Bird–Carreau viscous model ( $T_1 = 2[\eta_\infty + (\eta_0 - \eta_\infty)(1 + \lambda^2 \dot{\gamma}^2)^{(n-1)/2}]D$ ) fluids with  $\eta_0 = 100000$  and  $\eta_1 = 11111.1$  poise at several levels of shear thinning. Note that the steady shear profile of the Bird–Carreau model with  $\lambda = 60$  and  $n = 0.2$  is nearly identical to that of the single mode PTT model used in this work with  $\lambda = 100$ .

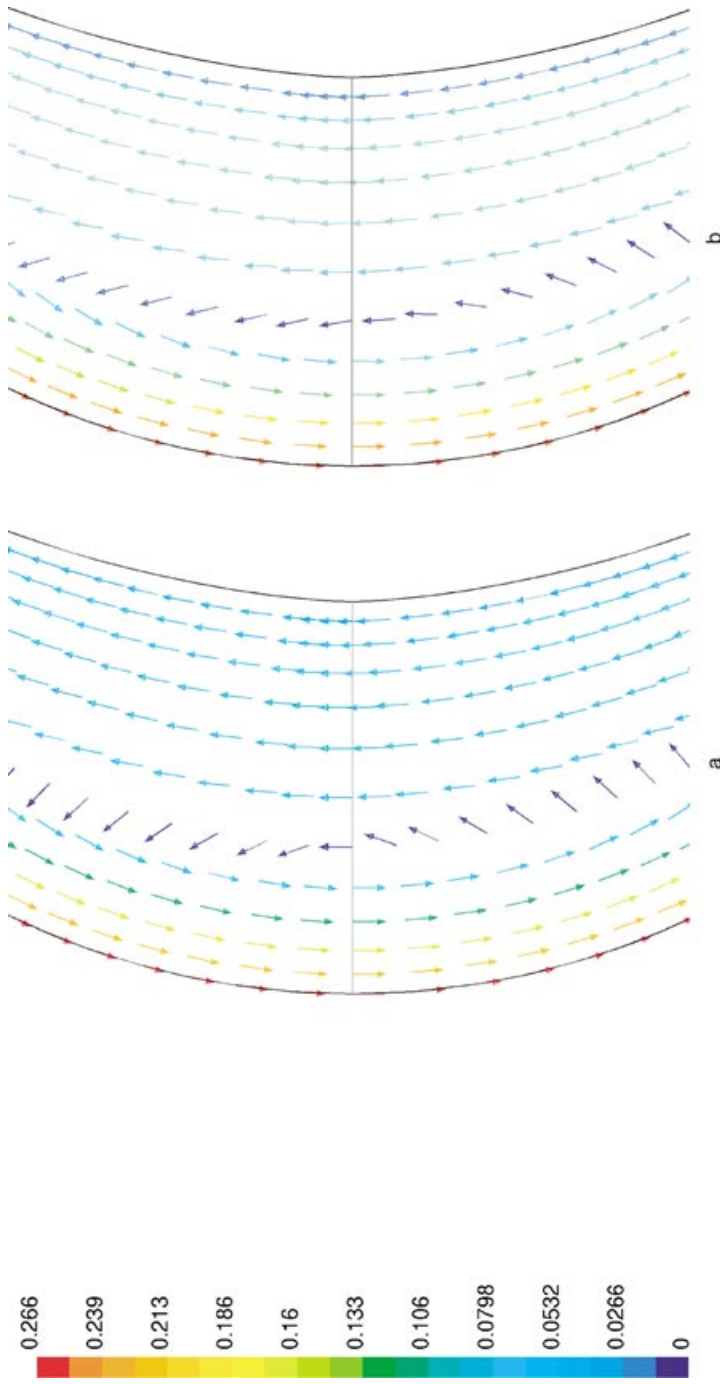


**FIGURE 7.** Velocity vectors colored according to magnitude at 1 rpm in the middle of the flow domain for relaxation times of (a) 0 s (Newtonian case) and (b) 100 s where the units of velocity are cm/s.

## 2-D NUMERICAL SIMULATION OF VISCOELASTIC FLUIDS IN A SINGLE-SCREW MIXER

viscoelastic effects are more apparent in the secondary profile.<sup>30</sup> In this case, the velocity profile consists of a central point around which the bulk of fluid is circulating as shown in Fig. 7 and some fluid flowing through the gap, with dead zones just before and behind the blade tip where the flow splits between the main circulating flow and the flow through the gap as shown in Fig. 8. The asymmetry is evident in the center of circulation, which moves toward the front of the blade with increasing viscoelasticity as shown in Fig. 7b. Also, the blade tip dead zones

are symmetric in the Newtonian case, but become increasingly asymmetric with increased viscoelasticity as demonstrated in Fig. 8b. The velocity divided by the time per revolution profile at  $x = 0$  is shown in Fig. 9. Note that the most distortion of the profile due to viscoelasticity is found with the 0.5 s relaxation time material and gradually returns to a profile similar to the Newtonian material as the relaxation time increases at 1 rpm. This is in spite of the fact that the pressure decreases substantially due to shear thinning, thus decreasing the pressure differential

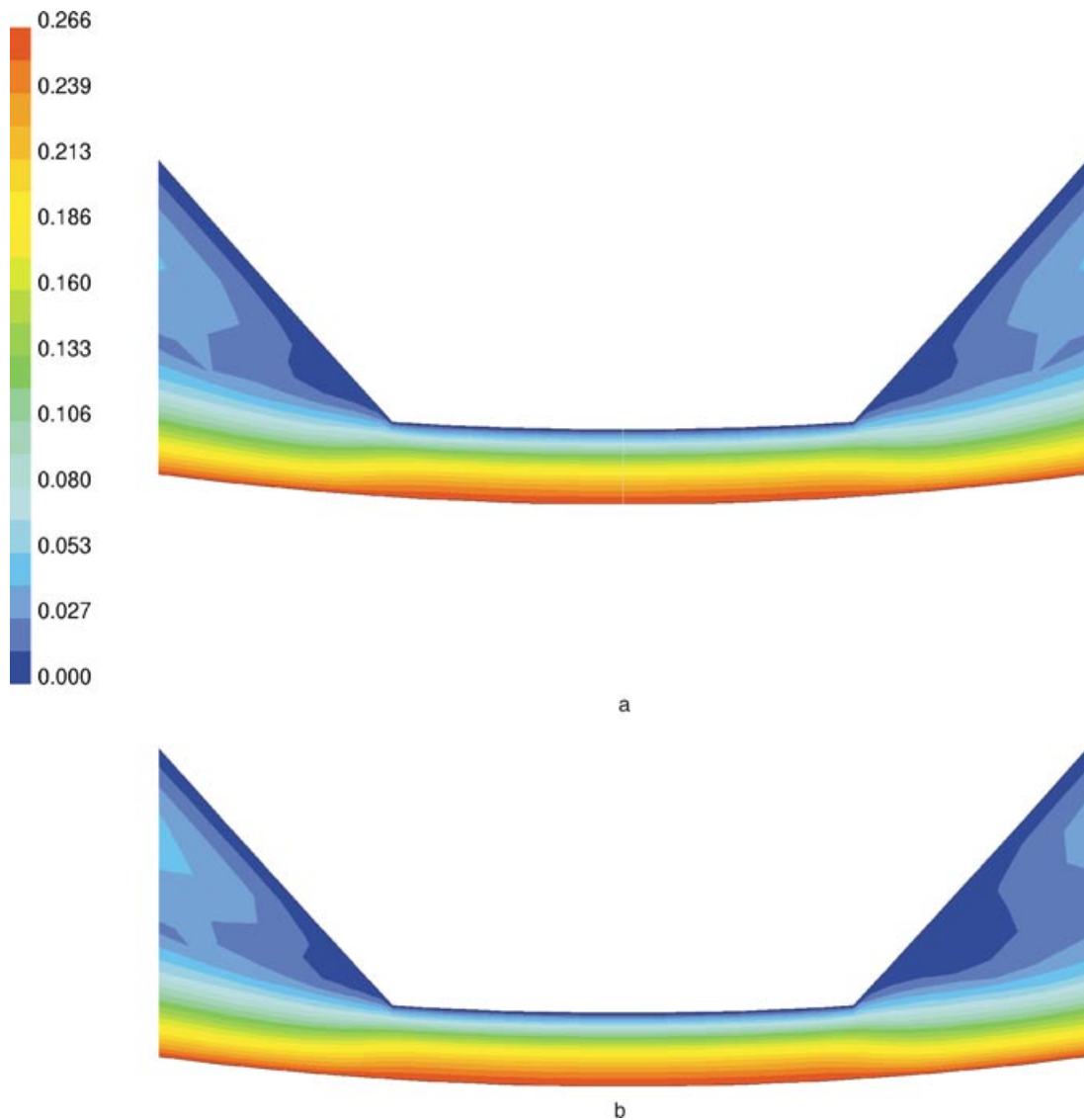


**FIGURE 8.** Velocity magnitude distribution at 1 rpm in the gap region for relaxation times of (a) 0 s (Newtonian case) and (b) 100 s where the units of velocity are cm/s.

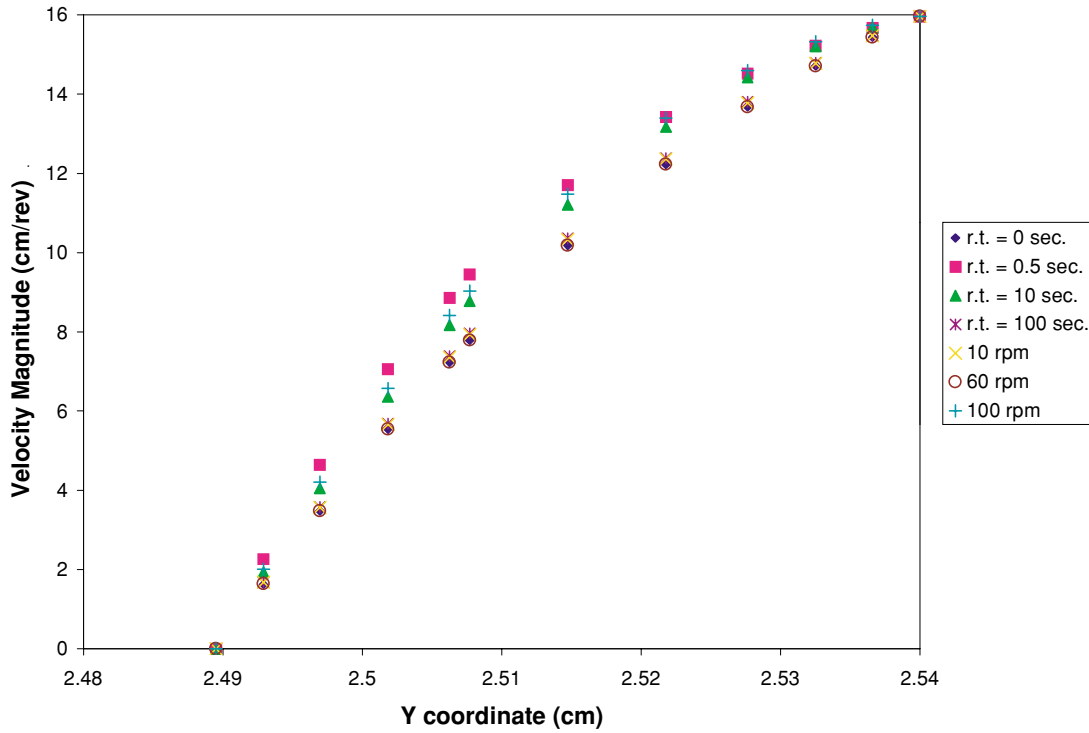


**FIGURE 9.** Velocity (cm/s) divided by the blade speed (rev/s) across the gap on the  $X = 0$  cm line at 1 rpm or at a relaxation time of 100 s unless otherwise noted.

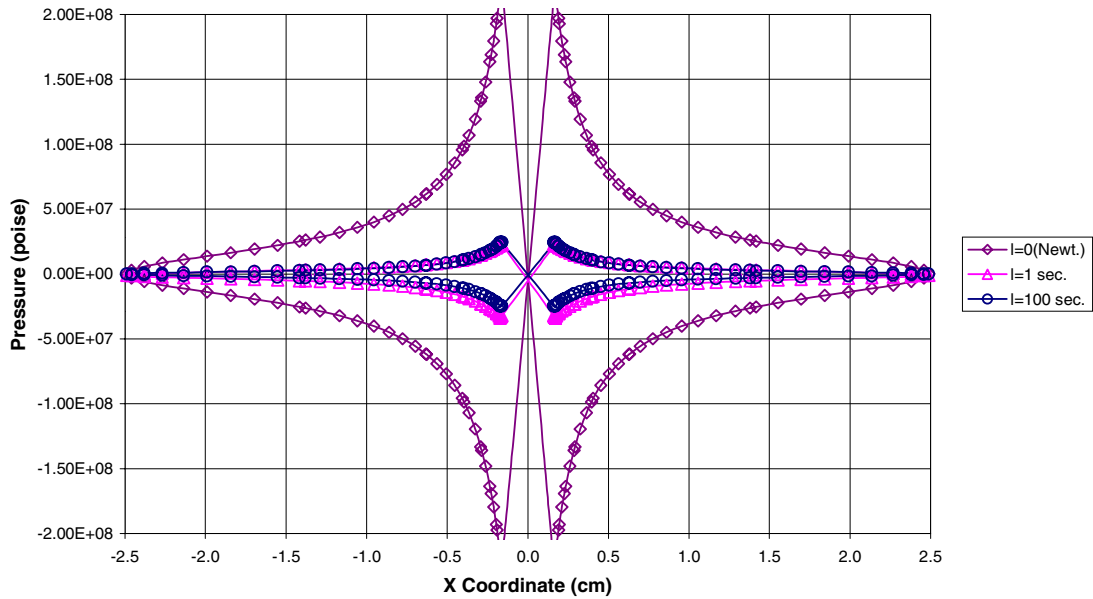


**FIGURE 10.** Pressure profiles at 100 rpm on the 2.489 cm radius circle with the 1480 element mesh for the PTT at several relaxation times.

## 2-D NUMERICAL SIMULATION OF VISCOELASTIC FLUIDS IN A SINGLE-SCREW MIXER

resistance to the flow. The flow through a gap in one revolution is 2.5–3% of the overall material, as calculated by taking the sum over the gap of the average velocity between two points multiplied by the distance between the points, dividing by the time per revolution, and then comparing the result to the total flow area. Viscoelastic effects appear to enhance flow through the gap slightly in accordance with the amount of distortion seen in the velocity profile.

As the blade velocity increases, the velocity profile in the gap at a relaxation time of 100 s remains

stable until 100 rpm, where inertia starts to become significant. Also, the effects of the viscoelasticity are less visible in the pressure and velocity profiles at 100 rpm and  $\lambda = 100$  s as shown in Figs. 10 and 11b, again indicating that the Newtonian component is dominating at this relaxation time as discussed previously. In contrast, at  $\lambda = 1$  s the 100 rpm profiles (see Figs. 10 and 11a) are similar in shape to those at 1 rpm with  $\lambda = 100$  s (see Figs. 5 and 8b), which is where the  $De$  is equivalent.

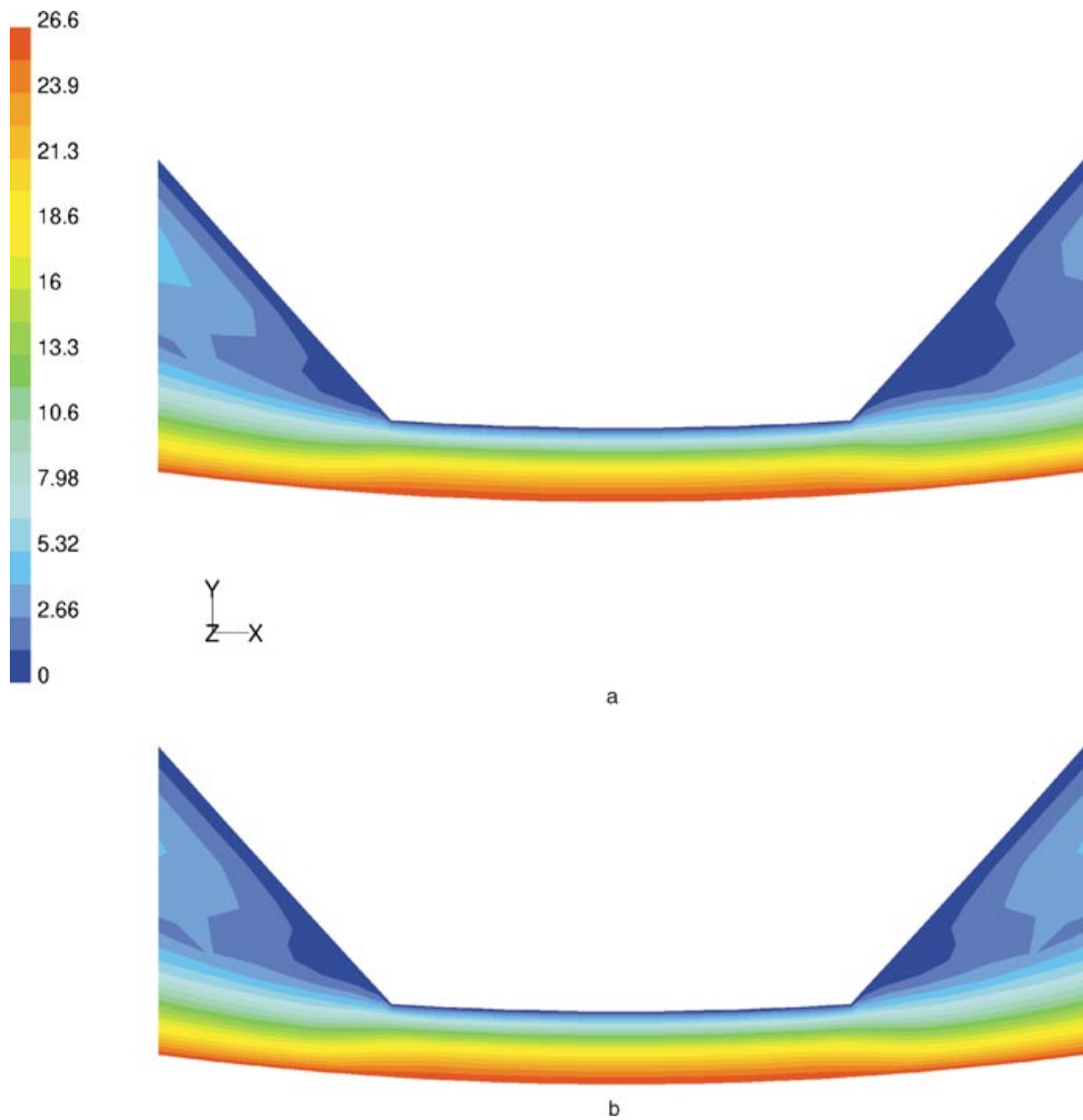


**FIGURE 11.** Velocity magnitude distributions at 100 rpm in the gap region for relaxation times of (a)  $\lambda = 1$  s and (b)  $\lambda = 100$  s where the units of velocity are cm/s.

2-D NUMERICAL SIMULATION OF VISCOELASTIC FLUIDS IN A SINGLE-SCREW MIXER

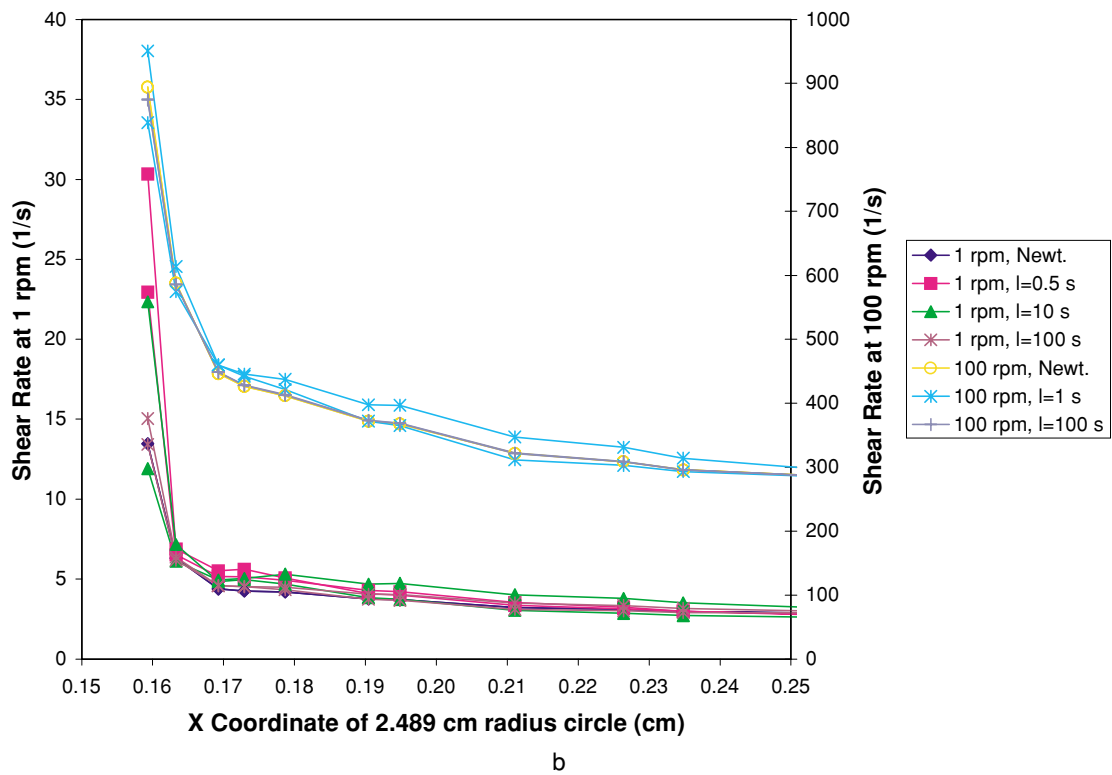
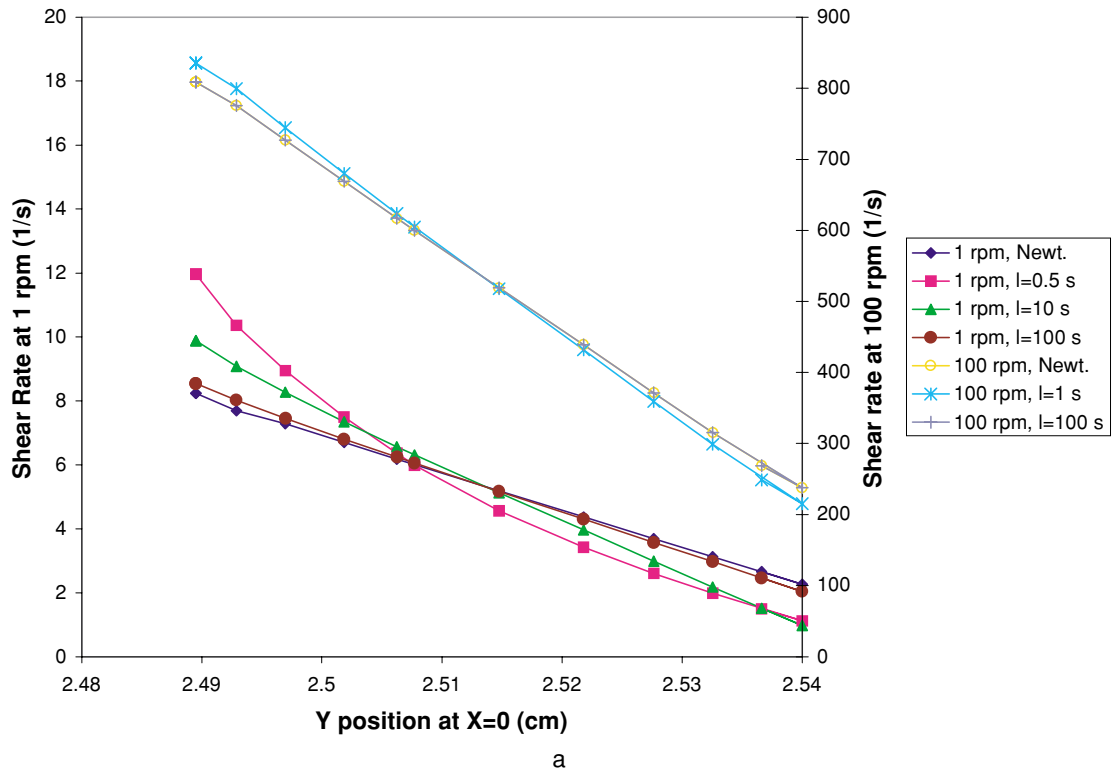


**FIGURE 12.** Effect of relaxation time of the PTT model on the shear rate (a) in the gap at the  $x = 0$  line and (b) near the blade tips on the 2.489 cm radius.

## 2-D NUMERICAL SIMULATION OF VISCOELASTIC FLUIDS IN A SINGLE-SCREW MIXER

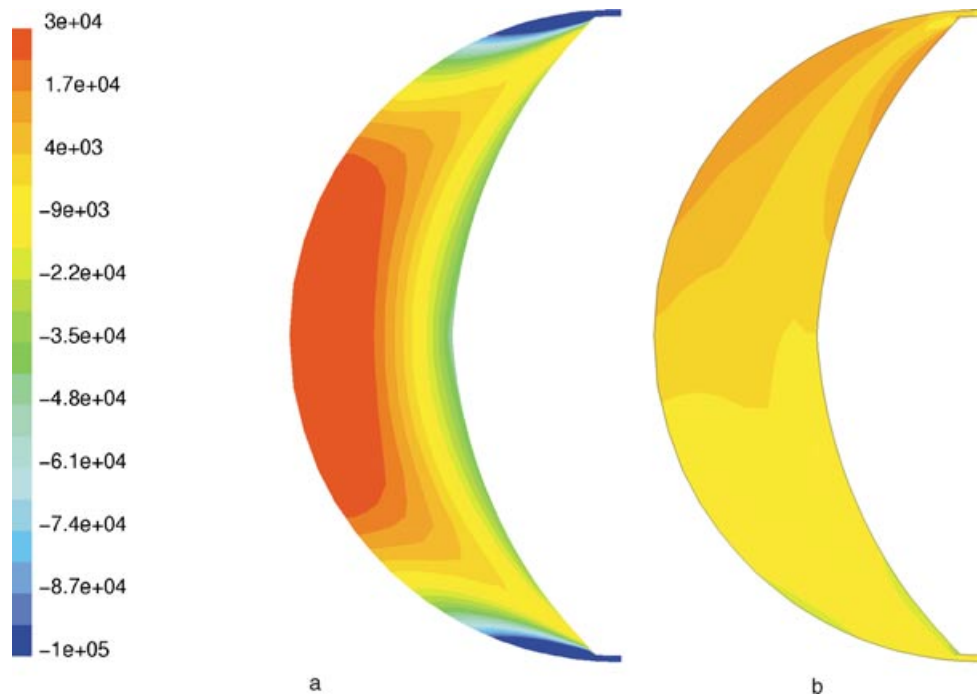


**FIGURE 13.** Shear stress distributions at 1 rpm for relaxation times of (a) 0 s (Newtonian case) and (b) 100 s where the units of stress are  $\text{gm/cm}^2$ .

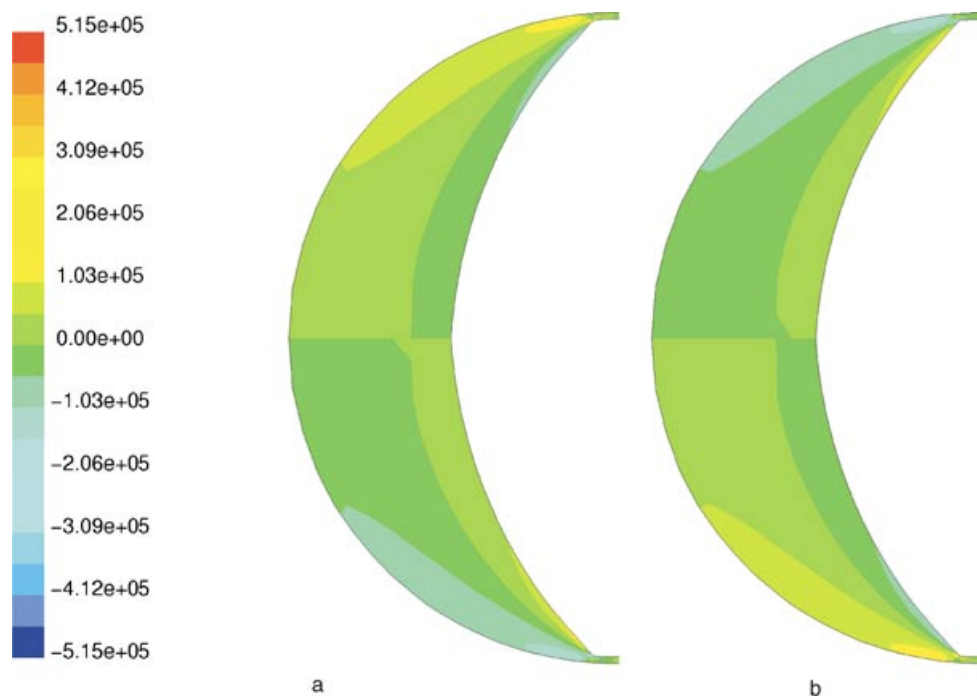


**FIGURE 14.** Normal stress distributions at 1 rpm for a Newtonian fluid ( $\lambda = 0$  s), (a)  $\tau_{11}$  and (b)  $\tau_{22}$  where the units of stress are  $\text{gm/cm}^2$ .

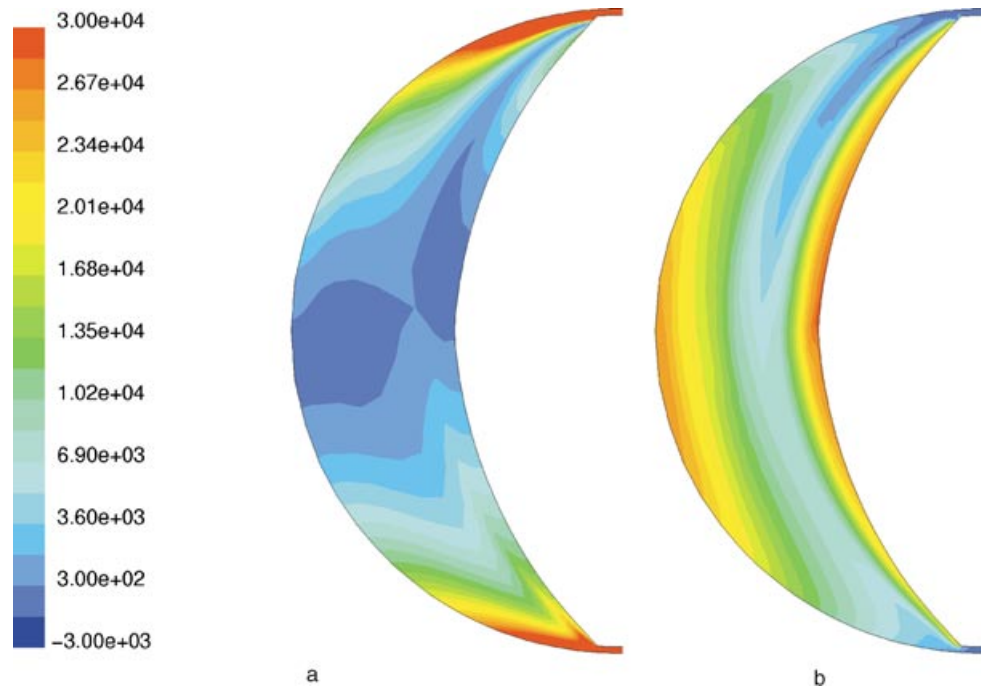


**FIGURE 15.** Normal stress distributions at 1 rpm for a relaxation time of  $\lambda = 100$  s, (a)  $\tau_{11}$  and (b)  $\tau_{22}$  where the units of stress are  $\text{gm/cm}^2$ .

The shear rate in the flow domain is low, except near the blade tip and in the gap. Shear rates in the gap and approaching the front and backsides of the on a circle of 2.489 cm are shown in Fig. 12. From the steady shear profiles in Fig. 3, it is seen that for  $\lambda = 0.5, 10$  and 51 s, the models are in the shear thinning regions at 1 rpm. In contrast, the Newtonian  $\lambda = 0$  has a constant viscosity of  $\eta_0$  and when  $\lambda = 100$  s the shear rate is such that a constant viscosity of  $\eta_\infty$  has been achieved in the gap. This is reflected in the way the shear rate varies in the gap in Fig. 12a, with the constant viscosity fluids linear and the shear thinning fluids curved. The slightly viscoelastic  $\lambda = 0.5$  s fluid has a much higher shear rate at the tip than the Newtonian or long relaxation time fluids, reflecting the differences in the pressure profile at this relaxation time noted earlier. The viscoelastic fluids have asymmetry in their shear rate profiles also, with higher shear rates at the front of the blade seen in Fig. 12b.

Changes in the stress distributions with the addition of viscoelasticity are dramatic as shown in Figs. 13–15. For the Newtonian case shown in Fig. 13, the normal stresses are not zero since this is not a viscometric flow, but they are equal and opposite such that the first normal stress difference  $N_1 = |\tau_{11}| - |\tau_{22}| \approx 0$ . The first normal stress difference varies

from zero near the corner singularity because of the error in the SU method. This error is not found for a Newtonian fluid solved using Galerkin's method without the use of SU. For the viscoelastic case, the expected power law relationship for  $\Psi_1$  is seen as shown in Fig. 16. Comparisons of the simulation results with the PTT steady shear expression for the first normal stress coefficient calculated at the same shear rates show that the simulation results are qualitatively in agreement with the calculated results, especially when taking into account that this is not a viscometric flow simulation. The shear rates used are the second invariants of the rate of deformation tensors calculated in the simulation. At the higher shear rates that are found near the corner singularity, some deviation in the simulation data is apparent in the graph, which again is thought to be due to the error inherent in the SU method.

## Conclusions

The process of solving a flow problem in a mixer for a differential viscoelastic fluid, using FEM is laid out, with a thorough look at the issues involved in

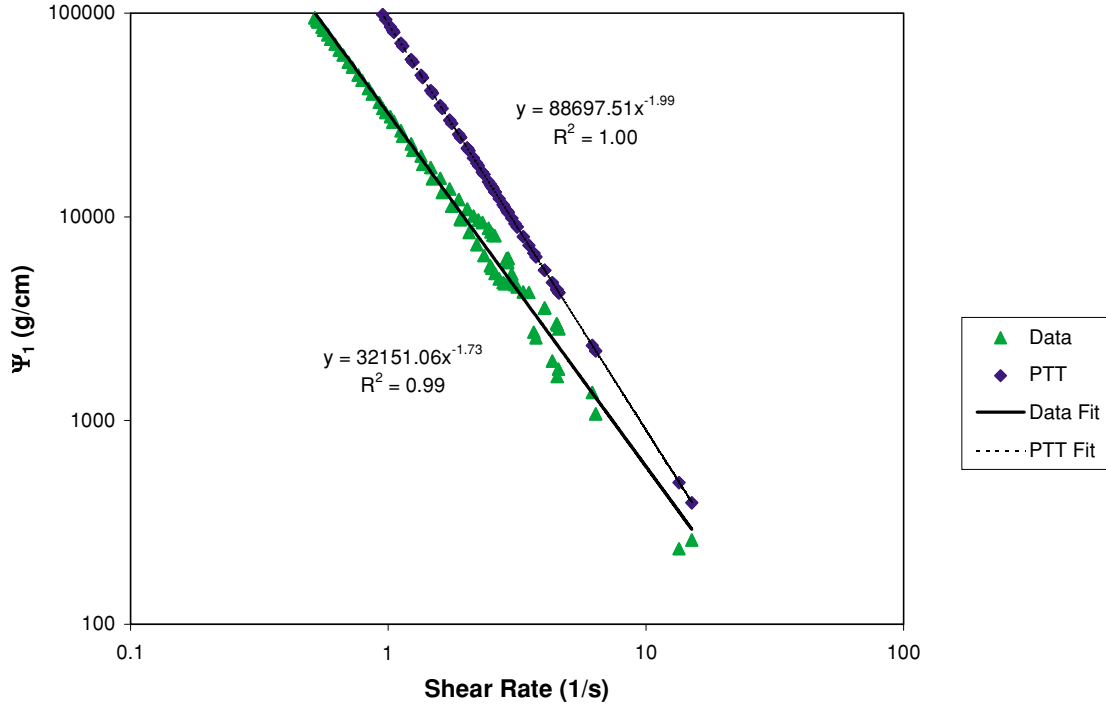


**FIGURE 16.** Primary normal stress difference ( $N_1$ ) vs. shear rate ( $\dot{\gamma}$ ) at 1 rpm for a relaxation time of  $\lambda = 100$  s.

developing a mesh, choosing an appropriate technique to handle the instabilities inherent in differential viscoelastic fluid models, understanding the error in the solution, and analysis of the data in terms that apply to mixers. Of the techniques available to us for the handling of differential viscoelastic fluid models, only the SU with  $4 \times 4$  subelements for stress technique of Marchal and Crochet<sup>12</sup> was able to solve this problem with a level of viscoelasticity useful for the study of dough mixing. While the error of the SU method is evident near the corner singularity in all the meshes studied, throughout most of the flow domain the mesh discretization error is of negligible importance so that qualitatively all the meshes give similar information. The effect of increasing rpm is to increase the magnitude of all the variables including the shear rate, and therefore shift the important viscoelastic effects to lower relaxation times. The importance of inertial forces also increases at higher speeds and thus stabilizes the solution. Centrifugal and Coriolis forces were found to generally stabilize the solution of the viscoelastic problem, with non-negligible effects on all variables at higher values of the relaxation time. In contrast, they had no measurable effect on simulations with purely viscous models. The general effect of viscoelasticity shown

in this work is to introduce asymmetry into the pressure and flow profiles, as well as greatly modifying the stress profiles from those for the Newtonian case. There are also reductions in the magnitudes of the pressure and stresses that are due to shear thinning effects.

The implication of these results is that a useful simplifying approach to modeling a viscous, viscoelastic materials such as dough or synthetic polymers that have a spectrum of relaxation times and viscosities is to tailor the viscoelastic models to include only those parameters that affect the rheology in the shear rate range of interest. For example, since only relaxation times up to around 2 s are shear thinning in the shear rate range generated in this geometry at 100 rpm, higher relaxation times can be dropped since they would not be able to relax at this characteristic process time and therefore are not contributing to the viscoelastic or shear thinning effects. Also, the stabilizing Newtonian component would need only be set to a value that would take over at shear rates higher than those seen in the process of interest, rather than the actual infinite shear viscosity seen in experiments. These simplifications allow the challenges of FEM with differential viscoelastic fluid models to be overcome, while allowing the

exploration of the effects of real fluids in a realistic geometry.

## Acknowledgment

This is publication No. D10544-14-01 of the New Jersey Agricultural Experiment Station supported by the Center for Advanced Food Technology (CAFT). The Center for Advanced Food Technology is a New Jersey Commission on Science and Technology Center.

## References

- Anne-Archard, D.; Boisson, H. C. *Int J Numer Methods Fluids* 1995, 21, 75–90.
- Youcefi, A.; Gaudu, R.; Bertrand, J.; Anne-Archard, D.; Sengelin, M. In *Proceedings of the 1992 Institution of Chemical Engineers Research Event, Manchester, U.K., 1992*; pp. 377–379.
- Youcefi, A.; Anne-Archard, D.; Boisson, H. C.; Sengelin, M. *Trans ASME* 1997, 119, 616–622.
- Petera, J.; Nassehi, V. *Int J Numer Methods Fluids* 1996, 23, 117–1132.
- Nassehi, V.; Ghoreishy, M. H. R.; Freakley, P. K.; Clarke, J. *Plast Rub & Composites Proc & Appl* 1997, 26(3), 103–112.
- Khayat, R. E.; Derdouri, A.; Frayce, D. *Int J Numer Methods Fluids* 1998, 28, 815–840.
- Dhanasekharan, M.; Kokini, J. L. *J Food Proc Eng* 2000, 23, 237–247.
- Ferziger, J. H.; Peric, M. *Computational Methods for Fluid Dynamics*; Springer-Verlag: Berlin, 1996.
- Crochet, M. J.; Davies, A. R.; Walters, K. *Numerical Simulation of Non-Newtonian Flow*; Elsevier: Amsterdam, 1984.
- Crochet, M. J. *Rubber Chem Technol* 1989, 62, 426–455.
- Brown, R. A.; McKinley, G. H. *J Non-Newtonian Fluid Mech* 1994, 52, 407–413.
- Marchal, J. M.; Crochet, M. J. *J Non-Newtonian Fluid Mech* 1987, 26, 77–114.
- Fortin, M.; Pierre, R. *Comput Methods Appl Mech Eng* 1989, 73, 341–350.
- Brooks, A. N.; Hughes, T. J. R. *Comput Methods Appl Mech Eng* 1982, 32, 199–259.
- Lou, X.-L.; Tanner, R. I. *J Non-Newtonian Fluid Mech* 1989, 31, 143–162.
- Tanner, R. I.; Jin, H. *J Non-Newtonian Fluid Mech* 1991, 41, 171–196.
- Crochet, M. J.; Legat, V. *J Non-Newtonian Fluid Mech* 1992, 42, 283–299.
- Crochet, M. J.; Delvaux, V.; Marchal, J. M. *J Non-Newtonian Fluid Mech* 1990, 34, 261–268.
- Debbaut, B.; Marchal, J. M.; Crochet, M. J. *J Non-Newtonian Fluid Mech* 1988, 29, 119–146.
- Rajagopalan, D.; Armstrong, R. C.; Brown, R. A. *J Non-Newtonian Fluid Mech* 1990, 36, 159–192.
- Baaijens, F. P. T. *J Non-Newtonian Fluid Mech* 1993, 48, 147–180.
- Baaijens, F. P. T. *J Non-Newtonian Fluid Mech* 1998, 79, 361–385.
- Booy, M. L. *Polymer Eng Sci* 1978, 18(12), 973–984.
- Rauwendaal, C.; Osswald, T. A.; Tellez, G.; Gramann, P. J. *ANTEC* 1996, 128–135.
- Batchelor, G. K. *An Introduction to Fluid Dynamics*; Cambridge University Press: Cambridge, UK, 1967.
- Spalding, M. A.; Dooley, J.; Hyun, K. S.; Strand, S. R. *ANTEC* 1993, 1533–1541.
- Anonymous *Gambit I User's Guide*; Fluent Inc., Lebanon, NH, 1998.
- Phan-Thien, N.; Tanner, R. I. *J Non-Newtonian Fluid Mech* 1977, 2, 353–365.
- Dhanasekharan, M.; Huang, H.; Kokini, J. L. *J Texture Stud* 1999, 30(5), 603–623.
- Ulbrecht, J. J.; Carreau, P. *Mixing of Liquids by Mechanical Agitation*; Gordon and Breach: New York, 1985; Vol. 1, Ch. 4.
- Polyflow. *User's Manual, Theoretical Background, Version 3.8*; Place del'Universite 16, B-1348 Louvain-la-Neuve, Belgium, 2001.
- White, J. L.; Chankraiphon, S.; Ide, Y. *Trans Soc Rheol* 1977, 21(1), 1–18.
- Collias, D. J.; Prud'homme, R. K. *Chem Eng Sci* 1985, 40(8), 1495–1505.
- Nienow, A. W.; Elson, T. P. *Chem Eng Res Des* 1988, 66(1), 5–15.